Time-Lapse, in Situ Imaging of Ice Crystal Growth Using Confocal Microscopy

Moreno Marcellini, Cécile Noirjean, Dmytro Dedovets, Juliette Maria, Sylvain Deville

Time-lapse, in-situ imaging of ice crystal growth with confocal microscopy

Moreno Marcellini,* Cecile Noirjean,* Dmytro Dedovets,* Juliette Maria,* and Sylvain Deville*

Laboratoire de Synthese & Fonctionnalisation des Ceramiques, UMR3080 CNRS/Saint-Gobain, 550 avenue Alphonse Jauffret, 84306 Cavaillon, France

E-mail: moreno.marcellini@yahoo.it; ce.noirjean@gmail.com; dmytro.dedovets@saint-gobain.com; juliette.maria@saint-gobain.com; sylvain.deville@saint-gobain.com

Abstract

Ice crystals nucleate and grow when a water solution is cooled below its freezing point. The growth velocities and morphologies of the ice crystals depend on many parameters, such as the temperature of ice growth, the melting temperature and the interactions of solutes with the growing crystals. Three types of morphologies may appear: dendritic, cellular (or finger-like), or the faceted equilibrium form. Understanding and controlling which type of morphology is formed is essential in several domains, from biology to geophysics and materials science. Obtaining *in situ*, three dimensional observations without introducing artefacts due to the experimental technique is nevertheless challenging. Here we show how we can use laser scanning confocal microscopy to follow in real-time the growth of smoothed and faceted ice crystals in zirconium acetate solutions. Both qualitative and quantitative observations can be made. In particular, we

*To whom correspondence should be addressed

can precisely measure the lateral growth velocity of the crystals, a measure otherwise difficult to obtain. Such observations should help us understand the influence of the parameters that control the growth of ice crystals in various systems.

Introduction

Understanding and controlling the growth of crystals, and in particular of ice crystals, is of interest in many domains, from geophysics to biology or food engineering. In materials science, the growth of ice crystals in colloidal suspensions is used in processing routes called ice templating or freeze casting,[1] where the unidirectional growth of the crystals and their successive removal by sublimation is used to template porosity in various materials. The microstructure, architecture, and properties of these materials is related, to some extent, to the morphology of the crystals grown during freezing. The dimensions and shape of ice crystals can be controlled, for example, by the cooling rate, the temperature gradient, the concentration and the composition of additives and particles, the pH condition, or the presence of externally applied magnetic or electric field.[2,3] The growth of the ice crystals may exhibit three different morphologies: dendritic, cellular (finger-like), and smoothed and faceted structures,[4] described by Gibbs-Curie-Wulff equilibrium.[5] Two of such examples are given by snowflakes or ice crystals in saline solutions.[6]

Several additives have been proposed to control the growth morphologies of ice crystals, with various success. These additives can be water-soluble solutes (sucrose, ethanol, glycerol)[7] or polymers (PVA, PEG).[8] If these additives all affect, to some extent, the freezing point, growth kinetics, and morphologies of the ice crystals, the latter almost always adopt cellular or dendritic morphologies. A form of Gibbs-Curie-Wulff equilibrium could be achieved by using Ice-Binding Proteins in solution (also called Anti-Freeze Proteins AFPs). Ice shaping is the results of their binding to ice. The first proteins to be discovered were the Anti-Freeze Glyco-Proteins (AFGP) in Antartic fishes,[9–11] followed by the report of Duman *et al.*[12] of a helical peptide in the serum of winter flounder. Both AFPs and AFGPs

can control the freezing temperature, the crystal growth, and the size of ice crystals during freeze-thaw cycles[13] in the serum of fishes,[14] insects,[15] and plants[16] that experience sub-zero temperatures.

Zirconium acetate (ZrAc) and zirconium hydroxy-acetate (ZrHAc) are probably the only inorganic compounds that mimic the ice-faceting properties of AFPs.[17–19] The growth of ice crystals in presence of ZrAc probably occur under the Gibbs-Curie-Wulff equilibrium. ZrAc can thus be used as a simple model system to grow faceted crystals and measure their growth kinetics. ZrAc in water organizes in tetrameric stacks[20] which might mimic the repetitive motif of certain AFPs.[21,22]

Although several methods have been proposed to follow the growth of ice crystals *in situ*, none of them can provide 3D, real-time observations without affecting the system. Optical microscopy is limited to 2D, surface observations.[23] Computed X-rays tomography can provide time-lapse, 3D observations, but the local absorption of synchrotron X-rays increases the temperature and affects the growth behaviour and morphology of the ice crystals.[24] Optical interferometry has been used to track the freezing front, but cannot provide informations about the morphology of ice crystals.[25] Transmission electron microscopy can be used to image the growth of crystals and the behaviour of particles repelled by the latter, but such experiments cannot yet be run routinely and the interaction of the electron beam with the sample is always questionable.[26] Near infrared imaging spectroscopy was used to investigate the morphology of ice crystals in biological materials, but freezing was not done *in situ*, and the spatial resolution is still not sufficient to image small crystals.[27]

Here we show how confocal laser scanning microscopy and image analysis can be used to investigate the growth of ice crystals as small as tens of micrometers *in situ* in ZrAc solutions, stained with Sulforhodamine B, in a confined thin slab. We will show that we can follow and reconstruct the ice crystals topography, estimate quantitatively the kinetic of the advancing ice front while freezing with a table-top instrument.

Results

Freezing process

We first verified that, at this concentration, Sulforhodamine B has no effect on the morphology of the ice crystals. A sample of 60 μL of a pristine 1 mM Sulforhodamine B solution was diluted in 1 mL of deionized water. A sample of 12 μL was prepared and frozen. The results of the 3D-topography of the frozen solution at the temperature of ≈ -22 °C, cooled at $\Delta(T) = -1$ °C/min, is shown in Fig. 1.

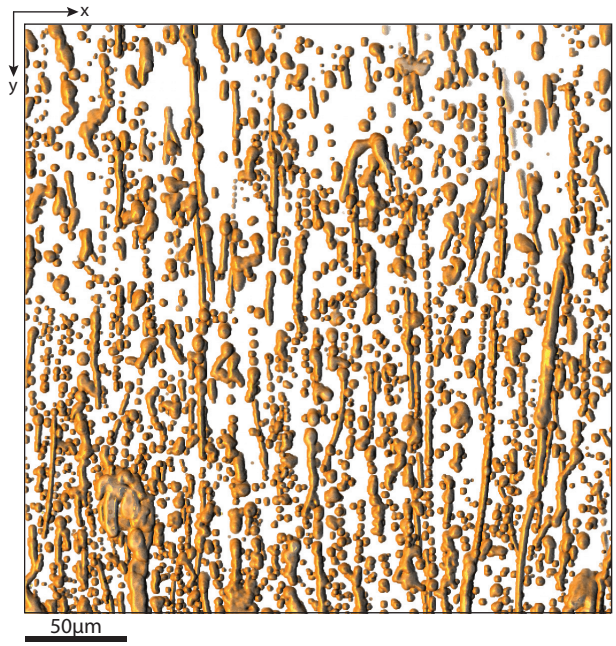

Figure 1: **3D-topography of brine channels (with Sulforhodamine B) in ice.** Visualisation of the trace of Sulforhodamine B cooled from room temperature to ≈ -22 °C at the rate of $\Delta(T) = -1$ °C/min. The fluorophore is expelled from the frozen water and concentrate in small, rounded pockets. Similar effect is found in freezing of salty water and the formation of brine pockets. The pockets are aligned along the freezing direction y. Thickness: 28 μm.

No regular structure is observable in the Sulforhodamine B trace. As expected, water, while freezing, rejects brine, which also contains the fluorophore accumulated at the grain boundaries.[6,28,29] With the proper fluorophore, we can thus quantitatively and thermodynamically follow the growth of ice crystals,[30] with or without ZrAc in solution.

The freezing of #2(TMA-OH) and #2(NaOH) solutions was observed as a function of time in the x-y plane at full cooling velocity to refine the sample position, to check the extent of condensation, and to capture the longitudinal dendritic growth of the ice crystals.

Generally no freezing was observed until the temperature of the Peltier stage was below -15 °C. Due to the supercooled state of the solution, the ice initially bursts in small dendritic crystals which densely populate the slab, hindering any observation. These crystals will grow until the temperature matches the equilibrium melting temperature T_m. This obliges us to carefully select the x-z plane to measure: to get an overall insight of the ice crystals geometries and growth kinetic we select *a priori* a plane where we expect that the Sulforhodamine B fluorescence will dominate over the transparency of the ice and we will observe a few large crystals. Because of the supercooling effects when cooling from room temperature, we opted for a seeding protocol. The solution is quickly frozen to trigger the nucleation of ice and the sample is then brought back to a temperature of -10 °C and thermalized for 10 minutes. The ice re-crystallizes at this temperature, leaving just a few crystals. We can then use these seeds to grow larger crystals in controlled conditions.

The supercooled state can be explained by lack of nucleation points, the colligative depression of the freezing point caused by the electrolyte, and by the confined state of the solution (analogous to similar effect in very small capillaries[31]). We believe that due to the confinement, the nucleating water must override a change in internal pressure. At the critical point of the water/ice phase transition, the ice faces a density change of $\approx -8\%$. This change in density must be accommodated either by changing the volume (fixed internal pressure) or by changing the internal pressure (at fixed volume). We hypothesize that a change in internal pressure occurs, and the excess of pressure is accommodated by lifting the top glass slide, that is, by increasing the volume: an effect similar to frost weathering (ice can exert pressures in the order of thousands of bars[32]). Due to this supercooled state and by observing small crystals after freezing burst, we speculate that in a free falling temperature experiment there are two stages for ice growth:[33] the rapid dendritic/cellular growth followed

by an apparent regular Gibbs-Curie-Wulff equilibrium growth when the crystals tips reach the position where $T = T_m$.

Imaging ice crystals

An example of what we can image both in the x-z and the x-y planes is shown in Fig. 2.

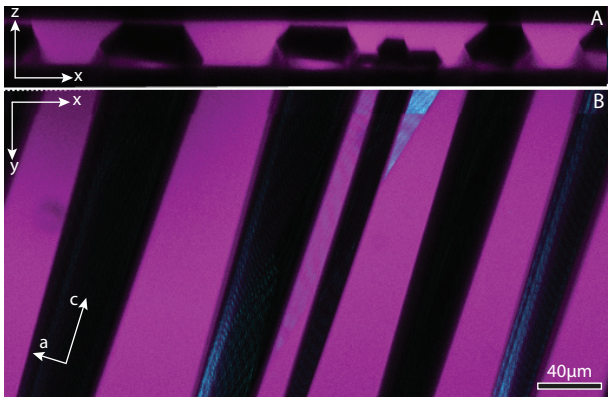

Figure 2: **Two dimensional view of ice crystals.** a) x-z plane: section of #2(NaOH) frozen at a ramp rate of $\Delta(T) = -1$ °C/min. Temperature gradient along z. b) One of the possible x-y views of the same sample showing the dark shadows of the ice crystals. Temperature gradient along y. The c and a-axis direction are indicated in the lower left.

The growth orientation on the x-y plane can be tilted with respect to the edge of the image (Fig. 2(b)). In the x-z plane, the ice crystals may thus be probed at a certain angle, which partially explain the elongated morphology of the crystals along the x direction (Fig. 2(a)).

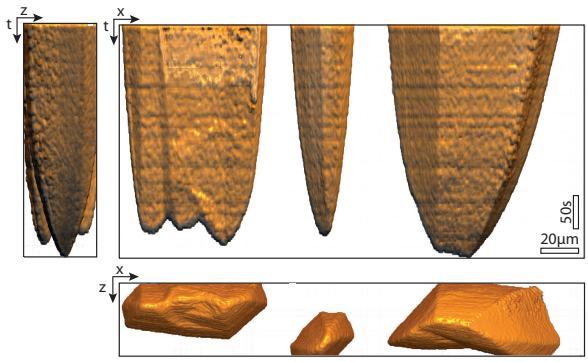

Figure 3: **Time-topography of ice crystals.** Three-dimensional time-topography visualising the growth of ice crystals in solution #2(NaOH) as function of time at the fixed cooling rate of $\Delta(T) = -1$°C/min. ZT, XT, and XZ views.

By collecting a series of similar images of the same x-z section as function of time (Fig. 2), the growth of ice crystals can be visualized as three-dimensional objects (Fig. 3).

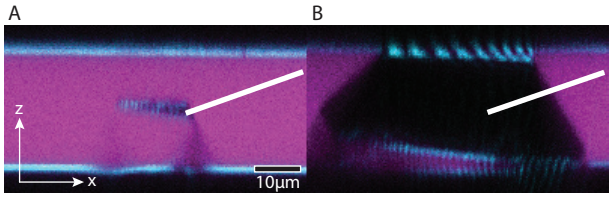

Figure 4: **Ice crystal evolution.** Transversal evolution of an ice crystal in #2(NaOH) at temperature rate of $\Delta(T) = -1$°C/min, without pre-seeding. a) at the reference time $t = 0$ b) after $t = 336$ s (121 frames). The white line represents the trajectory for computing the facet velocity.

We can use such series of images to measure the transversal and longitudinal growth velocities of the ice crystals. Let us consider two cross-sections at different times (Fig. 4) of the sample shown in Fig. 3. A straight line is drawn across the border between solution and ice such that the facet of the ice crystal moves perpendicular to this line. The series of frames is then re-sliced along the line without interpolation. The resulting image intensity is renormalized and binarized. A simple code written in Octave[1] searches for the edge and displays the results in term of length of trajectory and growth velocities.

Table 1: Table of the average v_t: $\Delta(T)$ in °C/min, v_t in μm/s.

$\Delta(T)$	#2(NaOH)	#2(TMA-OH)
-1	0.10 ± 0.03	0.07 ± 0.04
-2.5	0.10 ± 0.05	0.10 ± 0.05

From the analysis on several crystals grown in controlled freezing upon seeding, we can obtain a mean value of the transverse growth velocities v_t (table 1). For a cooling rate of $\Delta(T) = -1$ °C/min, the growth velocity in the TMA-OH solution is slightly lower than that in the NaOH solution. However, no differences are found for a cooling rate of $\Delta(T) = -2.5$ °C/min. The growth rate of the crystals in the NaOH solution is the same for the two cooling rates. We cannot at this point conclude whether the growth of the crystals is kinetic- or diffusion-limited. At this stage, the liquid water surrounding the crystals is

[1]GNU Octave, version 4.0.1 (2016) John W. Eaton *et al.*, www.octave.org

heavily charged in solutes which slow down the freezing. The solutes diffusion is very limited because of the low temperature and the already high solute concentration.

To better understand how the morphology of the ice crystal changes during its growth, we developed a Python code which searches for the liquid-crystal interface. Each frame is firstly filtered by a Gaussian filter which smooth the image, that is then segmented. Isocontours are drawn and the largest closed one is selected as the ice crystal area. Filter and detection of contours are obtained from the Skimage[34] and Trackpy[35] packages. The code developed to track the contours and compute the growth velocities is available on Figshare for anyone to review, reuse, improve, or adapt to something else.[36] In Fig. 5 the evolving contours of the central crystal from Fig. 3 are shown together.

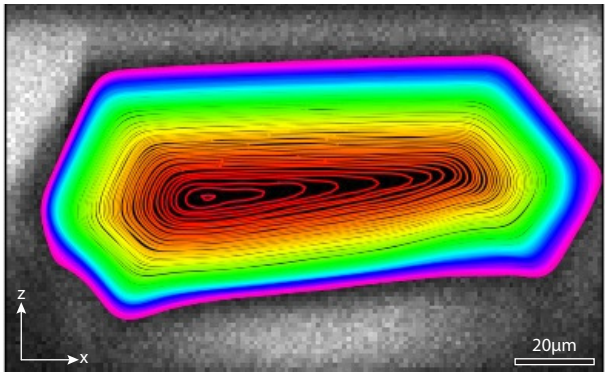

Figure 5: **Evolution of the contour of the ice crystal with time.** #2(NaOH) at $\Delta(T) = -1$ °C/min. The morphology of the crystal changes as function of time, from quasi-triangular to hexagonal.

The growth of the crystal follows several steps by changing its apparent geometry from quasi-triangular to hexagonal. The apparent geometry depends on the viewing angle, as exposed previously. In Fig. 6 we select 5 frames from Fig. 5 with different geometries.

From these contours we can measure the temporal evolution of the perimeter and area of the crystal as well as its growth velocity.

The results for 4 representative crystals grown from the #2(TMA-OH) solution cooled at $\Delta(T) = -1$ °C/min are shown in Fig. 7. The four crystals show similar growth dynamics. The same conclusion can be drawn from the instantaneous velocity results (Fig. 8). The

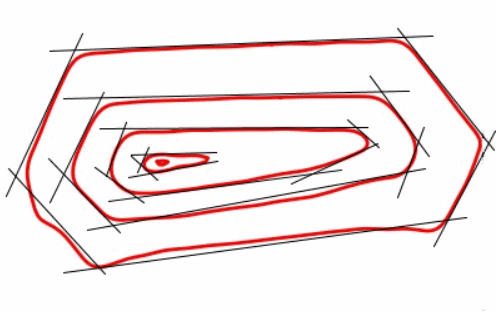

Figure 6: **Frames contours.** #2(NaOH) at $\Delta(T) = -1$ °C/min. Guides for the eyes through the different geometries.

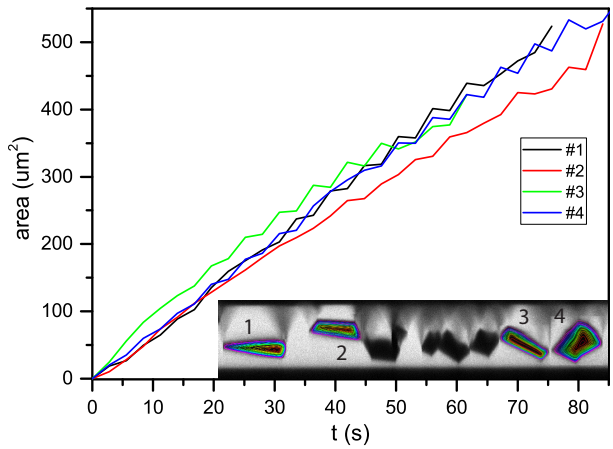

Figure 7: **Growth dynamics.** Area of individual crystals versus time. #2(TMA-OH) at $\Delta(T) = -1$ °C/min. The area was computed for the 4 crystals in the inset.

weighted average velocity v_A is of 6.1 ± 0.4 μm^2/s (computed here for one of the crystals).

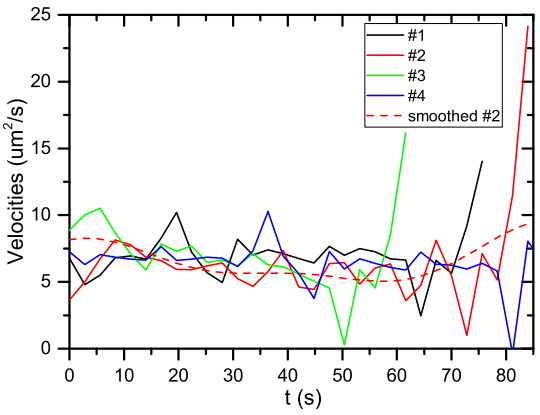

Figure 8: **Area velocity.** #2(TMA-OH) at $\Delta(T) = -1$ °C/min post-seeded. Area velocities computed from data in Fig. 7.

Nevertheless, we should stress that, because the cooling stage does not provide a good control of the temperature gradient, our measurements are somewhat position-dependent.

The same procedure was used to measure the longitudinal growth velocities v_l in both solutions. The values obtained for the two solutions and two cooling rates are given in Table 2.

Table 2: Table of the average v_l: $\Delta(T)$ in °C/min, v_l in μm/s.

$\Delta(T)$	#2(NaOH)	#2(TMA-OH)
-1	0.9 ± 0.4	0.9 ± 0.5
-2.5	2.4 ± 0.5	2.4 ± 0.4

The values of v_l only depends on the cooling rates: neither NaOH/HCl nor TMA-OH contents seem to play any role.

A typical 3D-topography of ice crystals grown from the #2(TMA-OH) solution (after final cooling at T = -21 °C) is shown in Fig. 9. Similar morphologies were obtained for all the solutions and cooling rates.

A more careful observation of single x-z images from the 3D-topography shows that single crystals can result from the effective merging of smaller ones protruding from the cold

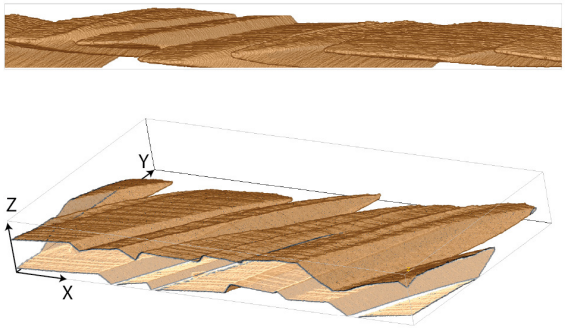

Figure 9: **Topography of ice crystals** 3D-topography of ice crystals grown from the #2(TMA-OH) solution cooled at $\Delta(T) = -1$ °C/min. The tips of the ice crystals look alike sharp chisels. Front view (top) and back view (bottom). Dimensions: 400 μm×200 μm×46 μm.

side: the sequence in Fig. 10 of 6 cross-sections illustrates such merging. In the first cross-section (namely "frame 1", where $\Delta y = 0$ μm represents the beginning of the sequence), we see 3 crystals, whose partial contours are highlighted by dotted lines. Two of them are already partially merged. At frames 18 and 47, that is we observe a cross-section at $\Delta y = 27.2$ μm and 73.6 μm from the beginning, the gap among the 3 crystals closes, so that at frame 72 ($\Delta y = 113.6$ μm) only one crystal is visible. Finally, at frame 95 ($\Delta y = 150.4$ μm) the geometry is perfectly hexagonal and shape and size are retained till frame 116 ($\Delta y = 184$ μm).

Discussion

The freezing point of the solution is of particular importance. The best results, in term of growing hexagonal crystals, can be achieved if, after the rapid freezing due to supercooling, one is able to bring back the solution to a temperature close to the melting point and melt until a few small crystals remain. In this case only the small remaining crystals will grow and the solute concentration in the liquid phase will closely approximate the concentration in the unfrozen solution. A similar method is generally used, for example, to distinguish single ice crystals grown in solution with Green Fluorescent Protein (GFP) tagged AFP [37,38] and to identify their positions with respect the ice faces. In the current experiments, we

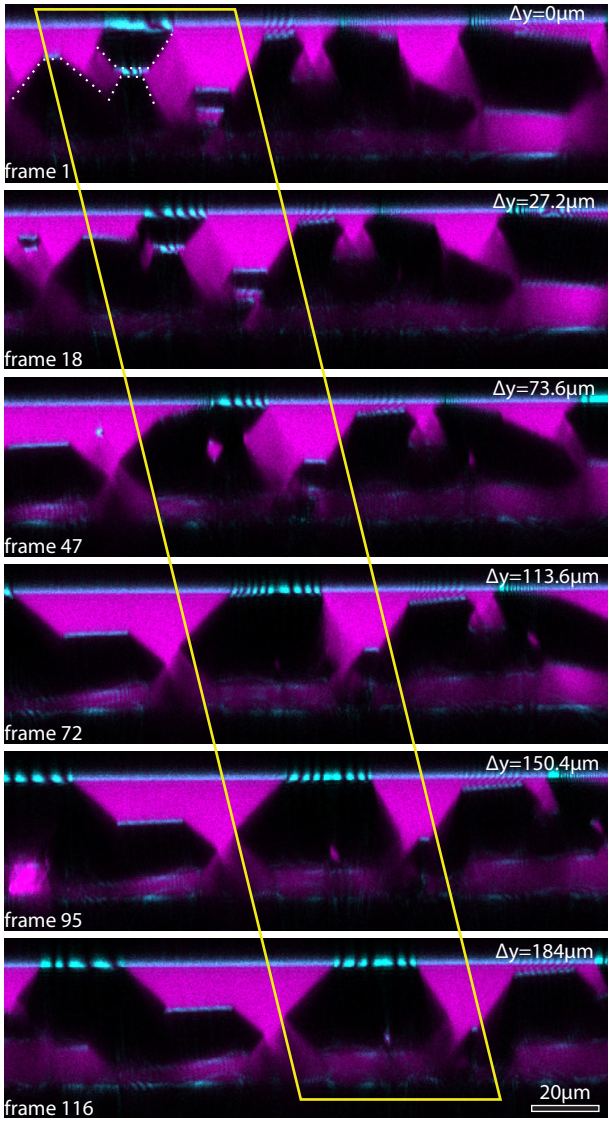

Figure 10: **Merging ice crystals.** Selected sections from a series of 3D-topography of ice crystals grown in the #2(TMA-OH) solution cooled at $\Delta(T) = -2.5$ °C/min. Top to bottom: the three crystals, highlighted by dotted contours on top sub-figure, merged into one and through an intermediate step become a single crystal with an hexagonal geometry.

cannot tag the ZrAc with a fluorophore because the fluorophore has to be smaller than the tagged molecules to avoid or reduce the interference with the kinetic and dynamic processes of freezing. Moreover, small fluorophores (such as the pyrene-based ones[39]) fluoresce under UV light that is unavailable for us with the current equipment, and tagging ZrAc with a fluorophore could limit the ability of ZrAc to self-assemble.

To better gauge and model the ice crystallization, the optical vertical resolution and the ability to isolate non-interacting crystals during the freezing should be optimized. Both conditions are inherent to the statistical analysis of velocities and morphologies. The ability to perform experiments with different liquid slab thickness should provide information on how the confinement affects the ice growth. If colloids are added to the initial solution of ZrAc,[18] the lateral ice growth is limited by the colloids engulfed between the crystals. Here, the lateral ice growth is only limited by the thickness of the slab and by the proximity of other ice crystals. Moreover, it seems that ice crystals do not prefer to grow in contact with the glass. We believe this is caused by the generation of brine which cannot escape because it accumulates between the ice and the two glass faces of the freezing chamber.

Phenomenologically, we can say that upon the rapid freezing and the subsequent thermalization ($T = T_m$), the mechanism of the crystal growth apparently follows the Gibbs-Curie-Wulff conditions while the crystal evolves along the thermal gradient. The ice crystals section expands monotonically, going through the shape change previously described, with a preference for the x-direction. This can be explained by the finite size of the liquid slab in the z axis, whereas the x- and y-direction seem infinite from the point of view of the ice crystal. It would thus be worthwhile to compute the surface free energy of the ice when in solution with and without ZrAc. Within our range of measurements and set-up, we cannot identify if the accretion of crystals is diffusion-limited or kinetic-limited.[40]

To perform an optimal experiment it is strongly needed to control the sample temperature with great precision, of the order of less than 0.1°C. We observed that the vertices of the ice crystals were the first to reshape when the temperatures became less stable. The tips,

in particular, are the weakest features. This observation raises the following question: if we model the ice needles as a pyramid on the top of a hexagonal prism (which correspond to the morphologies reported in presence of ice shaping proteins), what will be the maximum ratio between the basal plane and the pyramid height at thermodynamic equilibrium? And thus, which are the equilibrium crystallographic planes of ice in the presence of such additives? The observations obtained using the procedure described here could be used to validate or invalidate the different models proposed for this problem. ZrAc is easier to obtain and use than AFPs, it can thus be used as a model system to grow faceted ice crystals, difficult to achieve with other additives.

We hypothesize that, as proven,[20] ZrAc organizes in stacks, whose length is dependent on the concentration. Such stacks, through an adsorption mechanism similar to the one of antifreeze proteins, hinder the dendritic and cellular growth of ice crystals. The regular stacks intuitively resemble the repeating motif of several antifreeze proteins. The adsorption mechanism is mediated by the acetate anions. To follow where the ZrAc goes while water freezes, one could exchange one acetate with a small fluorophore, for example pyrene-based fluorophores,[39] whose size and weight are comparable with the ones of Zr tetramers (bearing in mind the limitations previously discussed on the length and weight of the fluorophore). In this way we may be able to track the dynamic of ZrAc clusters in proximity of the ice crystal and, by measuring the local fluorescence intensity be able to link the local density with the velocity of the ice front.[41] Similarly, we could identify how the ZrAc settles on the ice face, and if the mechanisms are indeed similar to that of AFPs.[42,43] Finally, by using a pH-sensitive fluorophore in solution we could quantitatively and thermodynamically follow the freezing process to gain further insight on how the pH distribution is linked to Zr tetramers and stacks.

Experimental methods

Experimental set-up

All the measurements were carried out with a Leica TCS SP8 (Leica-Mycrosystems, Mannheim, Germany) confocal laser scanning microscope. Confocal laser scanning microscopy has been primarily developed to image cells, proteins or other biological machines tagged with a fluorophore.[44] The technique is also of interest for studies in material science,[45] albeit rarely used so far.

The microscope is equipped with two external continuous laser sources, respectively at 488 nm (blue) and 552 nm (green) driven to the optical section by two independent optical fibres. The maximum powers on the optical plane are 10 mW for both of them. At these wavelengths the absorption coefficient for distilled water is $\approx 0.45 \cdot 10^{-3}$ cm^{-1} at 552 nm and $\approx 0.25 \cdot 10^{-3}$cm^{-1} at 488 nm.[46,47] The minimal absorption and the small intensities of both laser beams imply that no energy is deposited along the optical path through the sample of few tens of μm, as opposed to X-rays tomography where the intense and collimated beam may locally melt the ice or change the temperature gradient.[24,48] To focus the laser light at the region of interest, the sample stage is equipped with 3-axes micrometric drive. Sub-micrometer resolution for the z-axis (or vertical direction) is ensured by a galvanometric stage with a run of 200 μm.

The light-detection section includes a rotating head able to contain 6 objectives: two of the positions are occupied by a Leica HCX PL APO 40× dry objective and a Leica HCX PL APO CS 20× dry objective: working distances of both is 670 μm. This short length hampers the use of any encapsulating box filled with nitrogen to avoid the condensation of water on the top of the glass slide, such as in Ref. 37. The collected light is detected by two photomultiplier detectors which are fed with photons whose wavelengths can be independently selected. The smallest optical window is 5 nm, and the two spectra cannot overlap. With this set-up one can independently capture two fluorophores. The digitalization

of the integrated light is at 8-bits.

For the data collection the 20× objective was used to image the x-y plane and the x-z section for all the resolutions. For example, at a x-y hardware resolution of 1024×1024 px^2 (pixels^2), the area sampled is 775×775 μm^2 at the minimum optical magnification of $M = 0.75\times$ and frame rate of 0.388 frames/s with scanning frequency of 400 Hz, whereas for the x-z section a hardware resolution of 1024×256 px^2 gives a scanned section of 400×100 μm^2 at the minimum optical magnification of $M = 1.45\times$ and frame rate of 0.357 frames/s at a scanning frequency of 100 Hz. For the measurements in the x-z section, the optical plane is fixed and the sample is translated along the z-direction by the galvanometric stage. The microscope is controlled by the proprietary Leica LAS-AF software.

The sample stage was modified to accommodate a triple stage Peltier cooling device (Agilent Technologies), with water cooled back side connect to a chiller (Minichiller, Huber). The temperature on the sample side is measured by a Pt100 sensor and controlled by a Lakeshore 336 Temperature Controller that drives the current amplifier of the Peltier stage. With this set-up, the minimum temperature is -25 °C. However we can confidently reach a temperature in working conditions of ≥ -21 °C. Below this value, the temperature cannot be stabilized for times longer than few tens of minutes. The temperature measurement in the 0 to -21 °C range is accurate within 0.02 °C. The maximum linearly stabilized cooling rate is ± 5 °C/min. Faster cooling rates are possible initially, but the linearity is lost around -15 °C.

Sample preparation

A solution of zirconium acetate (in-house preparation of Saint-Gobain) at the initial concentration of 22.6 g/L (solution #1) of Zr (gravitometrically measured)[17] and original pH = 2.6 (measured by pre-calibrated Oregon Scientific pH-meter) was diluted in deionized water to obtain a solution with equivalent starting Zr concentrations of 13.3 g/L (pH = 3.2): two identical batches were prepared. This concentration was chosen because it is the lowest con-

centration at which ice faceting has been observed.[18] The pHs of one (#2(NaOH)) of the batches were then adjusted to pH $= 4.0 \pm 0.1$ by adding NaOH 25 mol/L solution and HCl solutions at 37% wt (Sigma Aldrich). The latter #2(TMA-OH) was carefully diluted with TMA-OH (tetramethylammonium hydroxide, Sigma Aldrich) at the concentration of 10% wt in water without overshooting pH ≈ 4. The objective was to titrate with two different base solutions to asses whether the ionic strength of the bases and the inorganic/organic nature of the bases influence the growth morphologies and/or kinetics. TMA-OH is a weak base (pK_b=4.2 versus pK_b=0.2 for NaOH). The final Zr concentrations for the TMA-OH solutions was estimated to 11.2 g/L.

Local gelation of the solutions was observed while adjusting with the bases: ZrAc eventually gelates at pH > 4.4. One night of stirring was enough for the complete solubilization of the gelated part. Each solution was stained with 1 mM Sulforhodamine B (Fluotechnik, France), 60 μL/mL. The absorption/emission spectra of Sulforhodamine B are rather insensitive to pHs in the range of 3 and 10,[49] and its absorption band is excited by the laser light at $\lambda = 552$ nm (absorption peak at $\lambda_{max} = 566$ nm and emission peak at $\lambda_{max} = 584$ nm in water). [2]

The fluorescent light is collected in the 575-625 nm range. To improve the image contrast at the liquid-solid interface, the reflected light of the blue laser ($\lambda = 488$ nm) is integrated in the 485-490 nm range. With respect to the method and set-up proposed by Neils *et al.*,[50] we image the ice-water interface through the optical axis.

The measured sample is prepared as following (Fig. 11): a 22×22 mm^2 microscope cover slide (borosilicate D263M, VWR, thickness $\approx$170 μm) is attached on the copper plate by vacuum grease which improves adhesion and thermal conductivity.

Half of the sample slide is in contact with the cold side of the stage (copper plate), while the other half is suspended in air because the copper plate is elevated above the surrounding metal plate, avoiding any contact on this side. 12 μL of ZrAc solution are deposited onto the

[2]Data from:
http://www.fluorophores.tugraz.at/substance/10

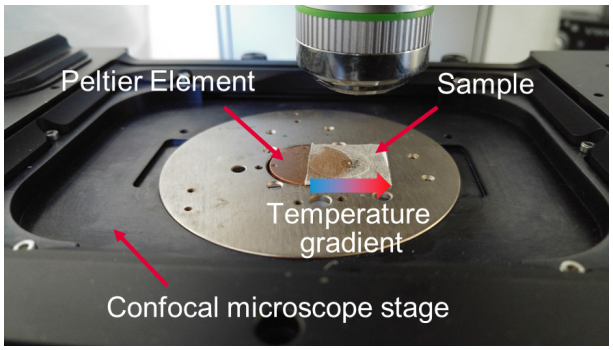

Figure 11: **Photograph of the sample set-up.** Half of the sample slide is on the cold side of the Peltier cell and the other half is suspended in air because the copper plate is elevated above the surrounding metal plate, thus there is no contact on this side. A temperature gradient parallel to the cover slip as well as perpendicular to its surface is thus created and ice crystals grow from the cold side towards the hot side of the sample.

middle of the cover slide. Another circular cover slide (15 mm diameter, ≈170 μm thickness) is deposited on top and sealed with nail polish. The sample thickness is constant for several hours. The nail polish is porous (after evaporation of the solvent) and observations showed that within 24 hours the solution eventually evaporated. The thickness of the liquid thin slab is $\delta \geq 40$ μm as measured by a x-z scan at the resolution of 1024×256 px^2. The imaging resolution affects the measurement of the thickness (Fig 12). To measure more precisely the slab thickness, the optical path should be carefully calibrated.[51] With the current sample preparation procedure, the estimated thickness for 12 μL of solution is $\approx$ 68 μm. Imaging with a squared resolution (same number of pixels in the x and z directions) provides thickness measurements close to the expected values.

With this set-up we create a longitudinal temperature gradient through the sample. To limit condensation, the sample and objective are surrounded by a transparent protective shield. In general, the imaging is carried out close enough to the edge of the copper plate. Condensation cannot however be avoided further on the cold side. We also regularly check for change in sample thickness: a sudden change may mean that the seal cracked during the freezing, in which case the sample is discarded.

By scanning the x-y plane (top-view) we can measure the longitudinal growth velocity

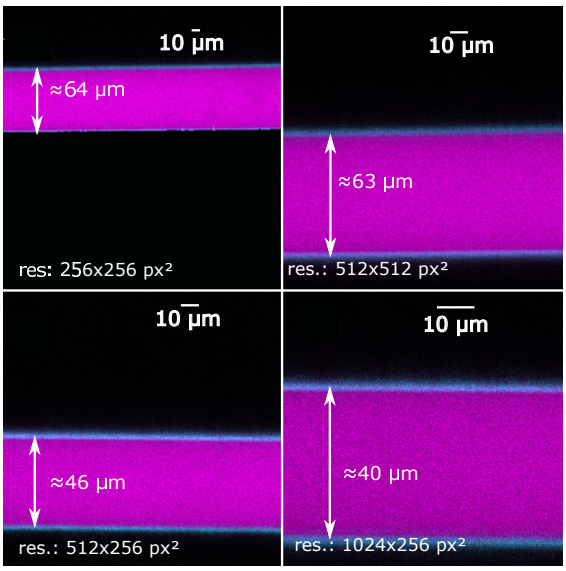

Figure 12: **Variations of the apparent measured thickness at various imaging resolutions.** To measure the true depth, the optical path should be carefully calibrated. The two squared resolutions give values close to the expected ones.

(v_l) of the ice crystals on the optical plane and by scanning the x-z plane (section view) we can measure the growth velocity of the edges (v_t) and their morphology. However, we cannot yet acquire time-lapse, three-dimensional images at a sufficient rate to perform the measurements in both directions at the same time. The data acquisition was thus performed in the following ways: we collected images

- of the x-y plane while cooling, to measure v_l (freezing direction y)
- of the x-z plane as function of time during the cooling to measure v_t
- at fixed temperature to obtain a 3D reconstruction of the crystals.

The gradient of temperature is thus along the y-direction, the thickness of the liquid slab is measured along the z-direction and the lateral size is measured along the x-direction.

Postprocessing and image analysis

The images are post-processed and analysed with Fiji.[52] The only digital manipulations done before the analysis are contrast enhancement and normalization in automatic mode. A cross-

section of the frozen sample #2(NaOH) is shown in two colours (Fig. 13): magenta represents the fluorescent signal from Sulforhodamine B diluted in water, while cyan is the reflected signal from different interfaces (top and bottom cover slides, and water/ice interfaces). The dark hexagon-like regions are ice crystals.

Figure 13: **Image of the sample section.** In magenta emission from water, in cyan reflection from liquid-glass interface. The black hexagon-like shades are ice crystals.

A qualitative analysis was performed on the time and spatial x-z series, which we can use to reconstruct the topography of the ice crystals, using Fiji.[53] The time-series (x-z-t axes) can be used to image the growth of ice crystal, while the spatial-series (x-y-z axes) show the three-dimensional topography. Image segmentation was performed using the Fiji built-in tools.

Conclusions

We demonstrate here how laser scanning confocal microscopy can be used to investigate *in situ* the three-dimensional growth of ice crystals, using a simple set-up and a fluorophore. The approach was done using a model system, an aqueous zirconium acetate (ZrAc) solution, that results in faceted growth of ice crystals. Upon freezing, in analogy with ice shaping proteins, ice crystals of predictable morphologies can develop in calibrated aqueous solutions. Because, like almost any solute, the fluorophore (Sulforhodamine B) is expelled by the growing crystals, the ice crystals appear as black bodies immersed in a sea of fluorescence. We were able to follow qualitatively and quantitatively the kinetic of the growing crystals with solubilized ZrAc tetramers. This methodology can also be used to investigate, for example, the growth in presence of simple polymers such as PVA, new promising ampholitic polymers,[54,55] either tagged or untagged with fluorophores, such as it has been proved with ice shaping proteins.[38,56,57] As a minimal amount of energy is deposited along the optical path in the sample, confocal microscopy appears much more appropriate than X-rays computed tomography, known to induce artefacts in the growth morphology of ice crystals.[24]

Funding

The research leading to these results has received funding from the European Research Council under the European Community's Seventh Framework Programme (FP7/2007-2013) Grant Agreement no. 278004 (project *FreeCo*).

Acknowledgement

M.M. wish to aknowledge Dr. G. Discepoli (@gd_roger) for the fruitful discussion in Peltier control.

References

(1) Deville, S. *Adv. Eng. Mater.* **2008**, *10*, 155–169.

(2) Porter, M. M.; Imperio, R.; Wen, M.; Meyers, M. A.; McKittrick, J. *Adv. Funct. Mater.* **2014**, *24*, 1978–1987.

(3) Tang, Y.; Qiu, S.; Miao, Q.; Wu, C. *Journal of the European Ceramic Society* **2016**, *36*, 1233–1240.

(4) Buckley, S. L.; Lillford, P. J. In *Modern Biopolymer Science*; Ubbink, S., Kasapis, I. T., Norton, J. B., Eds.; Academic Press: San Diego, 2009; pp 93–128.

(5) Li, R.; Zhang, X.; Dong, H.; Li, Q.; Shuai, Z.; Hu, W. *Advanced Materials* **2016**, *28*, 1697–1702.

(6) Untersteiner, N. In *The Geophysics of Sea Ice*, 1st ed.; Untersteiner, N., Ed.; Springer US, 1986.

(7) Fu, Q.; Rahaman, M. N.; Dogan, F.; Bal, B. S. *Journal of Biomedical Materials Research Part B: Applied Biomaterials* **2008**, *86*, 514–22.

(8) Deller, R. C.; Congdon, T.; Sahid, M. a.; Morgan, M.; Vatish, M.; Mitchell, D. a.; Notman, R.; Gibson, M. I. *Biomaterials Science* **2013**, *1*, 478.

(9) Somero, G. N.; DeVries, A. L. *Science* **1967**, *156*, 257–258.

(10) DeVries, A. L.; Wohlschlag, D. E. *Science* **1969**, *163*, 1073–1075.

(11) DeVries, A. L. *Cryobiology* **1970**, *6*, 585.

(12) Duman, J. G.; DeVries, A. L. *Nature* **1974**, *247*, 237–238.

(13) Jia, Z.; Davies, P. L. *Trends in Biochemical Sciences* **2002**, *27*, 101 – 106.

(14) Hew, C. L.; Fletcher, G. L.; Ananthanarayanan, V. S. *Can. J. Biochem.* **1980**, *58*, 377–383.

(15) Wu, D.; Duman, J. *Journal of Comparative Physiology B* **1991**, *161*, 279–283.

(16) Bravo, L. A.; Griffith, M. *Journal of Experimental Botany* **2005**, *56*, 1189–1196.

(17) Deville, S.; Viazzi, C.; Leloup, J.; Lasalle, A.; Guizard, C.; Maire, E.; Adrien, J.; Gremillard, L. *PLoS ONE* **2011**, *6*, e26474.

(18) Deville, S.; Viazzi, C.; Guizard, C. *Langmuir* **2012**, *28*, 14892–14898.

(19) Mizrahy, O.; Bar-Dolev, M.; Guy, S.; Braslavsky, I. *PLoS ONE* **2013**, *8*, e59540.

(20) Gossard, A.; Toquer, G.; Grandjean, S.; Grandjean, A. *Journal of Sol-Gel Science and Technology* **2014**, *71*, 571–579.

(21) Graether, S. P.; Gagné, S. M.; Spyracopoulos, L.; Jia, Z.; Davies, P. L.; Sykes, B. D. *Journal of Molecular Biology* **2003**, *327*, 1155–1168.

(22) Sun, T.; Lin, F.-H.; Campbell, R. L.; Allingham, J. S.; Davies, P. L. *Science* **2014**, *343*, 795–798.

(23) Anderson, A. M.; Grae Worster, M. *Journal of Fluid Mechanics* **2014**, *758*, 786–808.

(24) Deville, S.; Adrien, J.; Maire, E.; Scheel, M.; Di Michiel, M. *Acta Materialia* **2013**, *61*, 2077–2086.

(25) Butler, M. F. *Crystal growth & design* **2002**, *2*, 541–548.

(26) Tai, K.; Liu, Y.; Dillon, S. J. *Microscopy and microanalysis : the official journal of Microscopy Society of America, Microbeam Analysis Society, Microscopical Society of Canada* **2014**, *20*, 330–7.

(27) Do, G.; Araki, T.; Bae, Y.; Ishikura, K.; Sagara, Y. *Drying Technology* **2015**, *33*, 1614–1620.

(28) Lutzenkirchen, J.; Preocanin, T.; Kallay, N. *Phys. Chem. Chem. Phys.* **2008**, *10*, 4946–4955.

(29) Watanabe, H.; Otsuka, T.; Harada, M.; Okada, T. *J. Phys. Chem. C* **2014**, *118*, 15723–15731.

(30) Cheng, J.; Soetjipto, C.; Hoffmann, M. R.; Colussi, A. J. *J. Phys. Chem. Lett.* **2010**, *1*, 374–378.

(31) Liu, Z.; Muldrew, K.; Wan, R. G.; Elliott, J. A. W. *Phys. Rev. E* **2003**, *67*, 061602.

(32) Matsuoka, N.; Murton, J. *Permafrost and Periglacial Processes* **2008**, *19*, 195–210.

(33) Spannuth, M.; Mochrie, S. G. J.; Peppin, S. S. L.; Wettlaufer, J. S. *Phys. Rev. E* **2011**, *83*, 021402.

(34) van der Walt, S.; Schönberger, J.; Nunez-Iglesias, J.; Boulogne, F.; Warner, J.; Yager, N.; Gouillart, E.; Yu, T.; the scikit-image contributors, *PeerJ* **2014**, 2:e453.

(35) Allan, D.; Caswell, T. A.; Keim, N.; Boulogne, F.; Perry, R. W.; Uieda, L. trackpy: Trackpy v0.2.4. 2014; `http://dx.doi.org/10.5281/zenodo.12255`.

(36) Noirjean, C. Time lapse, in-situ imaging of ice crystal growth with confocal microscopy (Jupyter notebook). 2016; `https://figshare.com/s/7ae8c71c14326e911a5b`.

(37) Pertaya, N.; Marshall, C. B.; DiPrinzio, C. L.; Wilen, L.; Thomson, E. S.; Wettlaufer, J.; Davies, P. L.; Braslavsky, I. *Biophysical Journal* **2007**, *92*, 3663 – 3673.

(38) Drori, R.; Davies, P. L.; Braslavsky, I. *RSC Adv.* **2015**, *5*, 7848–7853.

(39) Tulock, J. J.; Blanchard, G. J. *J. Phys. Chem. B* **2002**, *106*, 3568–3575.

(40) Shibkov, A.; Golovin, Y.; Zheltov, M.; Korolev, A.; Leonov, A. *Physica A: Statistical Mechanics and its Applications* **2003**, *319*, 65–79.

(41) Zepeda, S.; Yokoyama, E.; Uda, Y.; Katagiri, C.; Furukawa, Y. *Crystal Growth & Design* **2008**, *8*, 3666–3672.

(42) Pertaya, N.; Marshall, C. B.; Celik, Y.; Davies, P. L.; Braslavsky, I. *Biophysical Journal* **2008**, *95*, 333 – 341.

(43) Bar-Dolev, M.; Celik, Y.; Wettlaufer, J. S.; Davies, P. L.; Braslavsky, I. *Journal of The Royal Society Interface* **2012**, *9*, 3249–3259.

(44) Pawley, J., Ed. *Handbook of Biological Confocal Microscopy*, 3rd ed.; Springer US, 2006.

(45) Hovis, D.; Heuer, A. *Journal of Microscopy* **2010**, *240*, 173–180.

(46) Hale, G. M.; Querry, M. R. *Appl. Opt.* **1973**, *12*, 555–563.

(47) Pope, R. M.; Fry, E. S. *Appl. Opt.* **1997**, *36*, 8710–8723.

(48) Schöder, S.; Reichert, H.; Schröder, H.; Mezger, M.; Okasinski, J. S.; Honkimäki, V.; Bilgram, J.; Dosch, H. *Phys. Rev. Lett.* **2009**, *103*, 095502.

(49) Coppeta, J.; Rogers, C. **1998**, *25*, 1–15.

(50) Neils, C. M.; Diller, K. R. *Journal of Microscopy* **2004**, *216*, 249–262.

(51) Besseling, T.; Jose, J.; van Blaaderen, A. *Journal of Microscopy* **2015**, *257*, 142–150.

(52) Schindelin, J. et al. *Nat Meth* **2012**, *9*, 676–682.

(53) Schmid, B.; Schindelin, J.; Cardona, A.; Longair, M.; Heisenberg, M. *BMC Bioinformatics* **2010**, *11*, 274.

(54) Mitchell, D. E.; Cameron, N. R.; Gibson, M. I. *Chem. Commun.* **2015**, *51*, 12977–12980.

(55) Mitchell, D. E.; Congdon, T.; Rodger, A.; Gibson, M. I. *Scientific Reports* **2015**, *5*, 15716–.

(56) Pertaya, N.; Celik, Y.; DiPrinzio, C. L.; Wettlaufer, J. S.; Davies, P. L.; Braslavsky, I. *Journal of Physics: Condensed Matter* **2007**, *19*, 412101.

(57) Drori, R.; Davies, P. L.; Braslavsky, I. *Langmuir* **2015**, *31*, 5805–5811.